Available online at www.sciencedirect.com
SCIENCE DIRECT®
International Journal of Thermal Sciences 44 (2005) 1047–1060
International Journal of Thermal Sciences
www.elsevier.com/locate/ijts

Numerical study of non-isothermal flow with convective heat transfer in a curved rectangular duct

S. Yanase [a,*], R.N. Mondal [b], Y. Kaga [c]

[a] *Department of Mechanical Engineering, Faculty of Engineering and Information Technology Center, Okayama University, Okayama 700-8530, Japan*
[b] *Graduate School of Natural Science and Technology, Okayama University, Okayama 700-8530, Japan*
[c] *Department of Computational Science and Engineering, Graduate School of Engineering, Nagoya University, Nagoya 464-8601, Japan*

Received 28 October 2004; received in revised form 10 March 2005; accepted 10 March 2005

Available online 23 May 2005

Abstract

Non-isothermal flow with convective heat transfer through a curved rectangular duct of aspect ratio 2 is numerically studied by use of the spectral method with a temperature difference between the vertical outer (heated) and inner (cooled) sidewalls. Numerical calculations are carried out for the Grashof numbers $100 < Gr \leqslant 1000$ over the Dean number $0 \leqslant Dn \leqslant 1000$. In the present paper, two cases of the Grashof numbers $Gr = 500$ and $Gr = 1000$ are discussed in detail. After a comprehensive survey over the parametric ranges, five branches of steady solutions are found using the Newton–Raphson iteration method for both the cases. Linear stability characteristics of each branch are then studied. It is found that among multiple steady solutions obtained, only one steady solution is linearly stable for a single range of the Dean number for $Gr = 500$, for $Gr = 1000$, on the other hand, linear stability region exists in three different intervals of the Dean number on the same branch. Nusselt numbers are calculated as an index of the horizontal heat transfer for differentially heated vertical sidewalls. It is found that the convection due to the secondary flow, enhanced by the centrifugal force, increases heat transfer significantly from the heated wall to the fluid, and whence the flow becomes periodic and then chaotic, as the Dean number increases, the rate of heat transfer increases remarkably with respect to a straight channel.

Keywords: Curved duct; Secondary flow; Convective heat transfer; Bifurcation; Dean number; Grashof number

1. Introduction

The study of flow through a curved duct is of fundamental interest because of its numerous applications in fluids engineering, such as in heat exchangers, ventilators, gas turbines, aircraft intakes and centrifugal pumps. The flow through a curved duct shows physically significant features under the action of the centrifugal force caused by the curvature of the duct. The presence of curvature generates centrifugal forces which act right angle to the main flow direction and produce secondary flows. One of the interesting phenomena of the flow through a curved duct is the bifurcation of the flow because generally there exist many steady solutions in the presence of channel curvature. Studies of the flow through a curved duct have been made, experimentally or numerically, for various shapes of the cross section. For example, for a circle (Dennis and Ng [1], Yang and Keller [2], Yanase et al. [3]), a semi-circle (Nandakumar and Masliyah [4]), an oval (Kao [5]) and a rectangle (Ligrani and Niver [6], Yanase and Nishiyama [7], Thangam and Hur [8] and Finlay and Nandakumar [9]). An extensive treatment of the bifurcation structure of the flow through a curved duct of rectangular cross section was presented by Winters [10] and Yanase et al. [11].

A remarkable characteristic of the flow through a curved duct is to enhance heat transfer to the fluid from two differentially heated sidewalls. However, experimental investigations of heat transfer in curved duct flows are limited because of the difficulties associated with the measurement

* Corresponding author. Tel.: +81 86 251 8226; fax: +81 86 251 8266.
E-mail address: yanase@mech.okayama-u.ac.jp (S. Yanase).

1290-0729/$ – see front matter
doi:10.1016/j.ijthermalsci.2005.03.013

Nomenclature

d	half width of the cross section of the duct
d_h	hydraulic diameter
Dn	Dean number
g	gravitational acceleration
G	mean pressure gradient
Gr	Grashof number
h	half height of the cross section of the duct
l	aspect ratio of the cross section
L	radius of the duct curvature
Nu	Nusselt number
Pr	Prandtl number
t	time
T	temperature
u	velocity component in the x-direction
v	velocity component in the y-direction
w	velocity component in the z-direction
x	horizontal axis
y	vertical axis
z	axis in the direction of the main flow

Greek letters

γ	coefficient of thermal expansion
δ	curvature of the duct
κ	thermal diffusivity
λ	resistance coefficient
μ	viscosity
ν	kinematic viscosity
ρ	density
ψ	sectional stream function

of fluid temperature profile, while corresponding numerical calculations are reported by many authors. In the studies of heat transfer in a curved channel, Cheng and Akiyama [12] and Mori et al. [13] numerically predicted steady, fully developed laminar forced convection in channels with uniform heat flux boundary conditions. Cheng and Akiyama [12] employed aspect ratio ranging from 0.2 to 5, whereas Mori et al. [13] used a square channel. In both investigations, temperature and velocity results showed clear evidence of secondary flows. Yee et al. [14] conducted numerical calculations to predict steady laminar flows with the boundary conditions of constant temperature in channels with aspect ratios of 0.33, 1 and 3 where no gravitational effect and hence no buoyancy effect was included. Komiyama et at. [15] presented numerical calculations to predict fully developed Nusselt numbers and secondary flows in a curved channel with no buoyancy influence. They treated channels of aspect ratios ranging from 0.8 to 5, and assumed constant heat flux boundary conditions. Ru and Chang [16] considered combined free and forced convections for fully developed flows in uniformly heated curved tubes. Ligrani et al. [17] studied channels of aspect ratio 40 and showed that the formation of secondary vortices is more affected by external heating at the outer wall than on the inner wall of the passage. Recently, Chandratilleke and Nursubyakto [18] performed numerical calculations to obtain secondary flows through curved rectangular ducts of aspect ratios 1 to 8, where the outer wall was heated. They studied for small Dean numbers, Dn, and compared the numerical results with their experimental data. Recently, Yanase et al. [19] studied the transition from steady flow to chaos via periodic states of isothermal and non-isothermal flows through a curved rectangular duct of aspect ratio 2 for a wide range of the Dean number. In the present paper, a numerical investigation is presented for the non-isothermal flows through a curved rectangular duct with a temperature difference between the vertical sidewalls for larger Grashof numbers ($100 < Gr \leqslant 1000$) over a wide range of the Dean number ($0 \leqslant Dn \leqslant 1000$). The effect of secondary flows on the heat transfer from the walls to the fluid is also studied by calculation of the Nusselt number.

2. Basic equations

Consider an incompressible viscous fluid streaming through a curved duct with a constant curvature. The cross section of the duct is a rectangle with width $2d$ and height $2h$. The flow is driven by a constant pressure gradient G along the center-line of the duct, i.e., the main flow in the z-direction (see Fig. 1). It is assumed that the flow is uni-

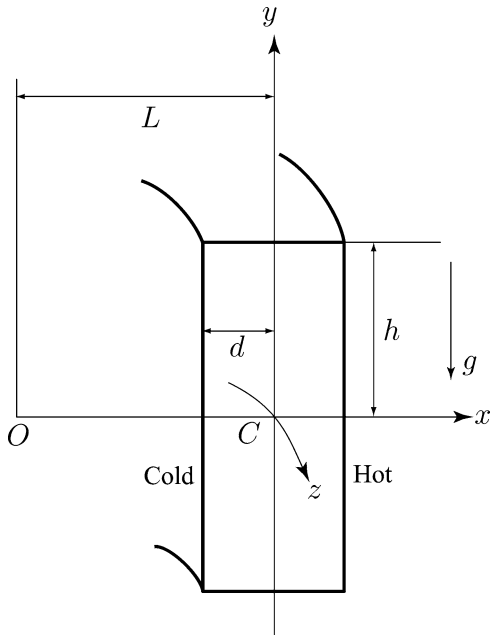

Fig. 1. Coordinate system of the curved rectangular duct.

form in the z-direction and that the outer sidewall is heated while the inner one is cooled. The temperature of the outer wall is $T_0 + \Delta T$ and that of the inner wall is $T_0 - \Delta T$ where $\Delta T > 0$. All the variables are non-dimensionalized by using the representative length d, the representative velocity $U_0 = \nu/d$, the representative time $d/U_0 = d^2/\nu$, where ν is the kinematic viscosity, and the representative temperature ΔT. Velocity components in the x- and y-directions are non-dimensionalized by U_0, and by $U_0/\sqrt{2\delta}$ in the z-direction, where $\delta = d/L$ is the curvature of the duct, L is the radius of the duct curvature, and temperature is non-dimensionalized by ΔT. Henceforth, all the variables are non-dimensionalized if not specified.

Velocity components in the x-, y- and z-directions are u, v and w respectively. Since the flow field is uniform in the z-direction, the sectional stream function ψ is introduced as

$$u = \frac{1}{1+\delta x}\frac{\partial \psi}{\partial y}, \qquad v = -\frac{1}{1+\delta x}\frac{\partial \psi}{\partial x} \tag{1}$$

A new coordinate variable y' is introduced in the y-direction as $y = ly'$, where $l = h/d$ is the aspect ratio of the duct cross section. From now on, y denotes y' for the sake of simplicity. The basic equations for w, ψ and T are then derived from the Navier–Stokes equations and the energy equation with the Boussinesq approximation as,

$$\begin{aligned}&(1+\delta x)\frac{\partial w}{\partial t} + \frac{1}{l}\frac{\partial(w,\psi)}{\partial(x,y)} - Dn + \frac{\delta^2 w}{1+\delta x}\\ &\quad = (1+\delta x)\Delta_2 w - \frac{\delta}{l(1+\delta x)}\frac{\partial \psi}{\partial y}w + \delta\frac{\partial w}{\partial x}\end{aligned} \tag{2}$$

$$\begin{aligned}&\left(\Delta_2 - \frac{\delta}{1+\delta x}\frac{\partial}{\partial x}\right)\frac{\partial \psi}{\partial t}\\ &\quad = -\frac{1}{l(1+\delta x)}\frac{\partial(\Delta_2\psi,\psi)}{\partial(x,y)} + \frac{\delta}{l(1+\delta x)^2}\\ &\qquad \times\left[\frac{\partial \psi}{\partial y}\left(2\Delta_2\psi - \frac{3\delta}{1+\delta x}\frac{\partial \psi}{\partial x} + \frac{\partial^2\psi}{\partial x^2}\right) - \frac{\partial \psi}{\partial x}\frac{\partial^2\psi}{\partial x\partial y}\right]\\ &\qquad + \frac{\delta}{(1+\delta x)^2}\left[3\delta\frac{\partial^2\psi}{\partial x^2} - \frac{3\delta^2}{1+\delta x}\frac{\partial \psi}{\partial x}\right]\\ &\qquad - \frac{2\delta}{1+\delta x}\frac{\partial}{\partial x}\Delta_2\psi + \frac{1}{l}w\frac{\partial w}{\partial y}\\ &\qquad + \Delta_2^2\psi - Gr(1+\delta x)\frac{\partial T}{\partial x}\end{aligned} \tag{3}$$

$$\frac{\partial T}{\partial t} + \frac{1}{l(1+\delta x)}\frac{\partial(T,\psi)}{\partial(x,y)} = \frac{1}{Pr}\left(\Delta_2 T + \frac{\delta}{1+\delta x}\frac{\partial T}{\partial x}\right) \tag{4}$$

where

$$\begin{aligned}&\Delta_2 \equiv \frac{\partial^2}{\partial x^2} + \frac{1}{l^2}\frac{\partial^2}{\partial y^2}\\ &\frac{\partial(f,g)}{\partial(x,y)} \equiv \frac{\partial f}{\partial x}\frac{\partial g}{\partial y} - \frac{\partial f}{\partial y}\frac{\partial g}{\partial x}\end{aligned} \tag{5}$$

The Dean number Dn, the Grashof number Gr and the Prandtl number Pr which appear in Eqs. (2)–(4) are defined as

$$Dn = \frac{Gd^3}{\mu\nu}\sqrt{\frac{2d}{L}}, \qquad Gr = \frac{\gamma g \Delta T d^3}{\nu^2}, \qquad Pr = \frac{\nu}{\kappa} \tag{6}$$

Here μ, γ, κ and g are the viscosity, the coefficient of thermal expansion, the coefficient of thermal diffusivity and the gravitational acceleration respectively. In the above formulation, five non-dimensional parameters l, δ, Dn, Gr and Pr are used. In the present study, Dn and Gr are varied while δ, Pr and l are fixed as $\delta = 0.1$, $Pr = 7.0$ (water) and $l = 2$.

The rigid boundary conditions for w and ψ are used as

$$\begin{aligned}&w(\pm1, y) = w(x, \pm1) = \psi(\pm1, y) = \psi(x, \pm1)\\ &\qquad = \frac{\partial \psi}{\partial x}(\pm1, y) = \frac{\partial \psi}{\partial y}(x, \pm1) = 0\end{aligned} \tag{7}$$

and the temperature T is assumed to be constant on the walls as

$$T(1, y) = 1, \qquad T(-1, y) = -1, \qquad T(x, \pm1) = x \tag{8}$$

It should be noted that Eqs. (2)–(4) are invariant under the transformation of the variables

$$\left.\begin{aligned} y &\Longrightarrow -y\\ w(x,y,t) &\Longrightarrow w(x,-y,t)\\ \psi(x,y,t) &\Longrightarrow -\psi(x,-y,t)\\ T(x,y,t) &\Longrightarrow -T(x,-y,t)\end{aligned}\right\} \tag{9}$$

Therefore, the case of heating the inner sidewall and cooling the outer sidewall can be deduced directly from the results obtained in this paper.

3. Method of numerical calculation

The method adopted in the present numerical calculation is the spectral method, in which variables are expanded in series of functions consisting of Chebyshev polynomials. That is, the expansion functions $\Phi_n(x)$ and $\Psi_n(x)$ are expressed as

$$\begin{aligned}\Phi_n(x) &= \left(1-x^2\right)C_n(x)\\ \Psi_n(x) &= \left(1-x^2\right)^2 C_n(x)\end{aligned} \tag{10}$$

where

$$C_n(x) = \cos\left(n\cos^{-1}(x)\right) \tag{11}$$

is the nth order Chebyshev polynomial. $w(x,y,t)$, $\psi(x,y,t)$ and $T(x,y,t)$ are expanded in terms of the functions $\Phi_n(x)$ and $\Psi_n(x)$ as

$$\left.\begin{aligned} w(x,y,t) &= \sum_{m=0}^{M}\sum_{n=0}^{N} w_{mn}(t)\Phi_m(x)\Phi_n(y)\\ \Psi(x,y,t) &= \sum_{m=0}^{M}\sum_{n=0}^{N} \psi_{mn}(t)\Psi_m(x)\Psi_n(y)\\ T(x,y,t) &= \sum_{m=0}^{M}\sum_{n=0}^{N} T_{mn}(t)\Phi_m(x)\Phi_n(y) + x\end{aligned}\right\} \tag{12}$$

where M and N are the truncation numbers of the polyno-

mial series in the x- and y-directions respectively. The expansion coefficients w_{mn}, ψ_{mn} and T_{mn} are then substituted into the basic Eqs. (2)–(4) and the collocation method is applied. As a result, the nonlinear algebraic equations for w_{mn}, ψ_{mn} and T_{mn} are obtained. The collocation points (x_i, y_j) are taken to be

$$x_i = \cos\left[\pi\left(1 - \frac{i}{M+2}\right)\right]$$
$$y_j = \cos\left[\pi\left(1 - \frac{j}{N+2}\right)\right] \tag{13}$$

where $i = 1, \ldots, M+1$ and $j = 1, \ldots, N+1$. The steady solutions are obtained by the Newton–Raphson iteration method and the convergence is assured by taking $\varepsilon_p < 10^{-10}$, where subscript p denotes the iteration number and ε_p is defined as

$$\varepsilon_p = \sum_{m=0}^{M}\sum_{n=0}^{N}\left[\left(w_{mn}^{(p+1)} - w_{mn}^{(p)}\right)^2 + \left(\psi_{mn}^{(p+1)} - \psi_{mn}^{(p)}\right)^2 + \left(T_{mn}^{(p+1)} - T_{mn}^{(p)}\right)^2\right]$$

In the present numerical calculations, $M = 20$ and $N = 40$ have been used to give sufficient accuracy of the solutions, which will be discussed in Section 5.1.1.

To solve the steady solution $\overline{w}(x, y)$, $\overline{\psi}(x, y)$ and $\overline{T}(x, y)$, the time derivative terms $\partial w/\partial t$, $\partial\psi/\partial t$ and $\partial T/\partial t$ are set to zero, and the expansion series (12) with coefficients w_{mn}, ψ_{mn} and T_{mn}, being time independent, is substituted into the basic Eqs. (2)–(4). Next, linear stability of the steady solutions is investigated against only two-dimensional (z-independent) perturbations. To do this, the eigenvalue problem is solved which is constructed by the application of the function expansion method together with the collocation method to the perturbation equations obtained from Eqs. (2)–(4). It is assumed that the time dependence of the perturbation is $e^{\sigma t}$, where $\sigma = \sigma_r + i\sigma_i$ is the eigenvalue with σ_r the real part, σ_i the imaginary part and $i = \sqrt{-1}$. If all the real parts of the eigenvalue σ are negative, the steady solution is linearly stable, but if there exists at least one positive real part of the eigenvalue, it is linearly unstable. In the unstable region, the perturbation grows monotonically for $\sigma_i = 0$ and oscillatorily for $\sigma_i \neq 0$.

Finally, in order to calculate unsteady solutions of the flow, the Crank–Nicolson and Adams–Bashforth methods together with the function expansion (12) and the collocation methods are applied to Eqs. (2)–(4). Though the present numerical calculations are carried out for the Grashof numbers $100 < Gr \leqslant 1000$ over the range of the Dean number $0 \leqslant Dn \leqslant 1000$, in the present paper, however, two cases (i) $Gr = 500$ and (ii) $Gr = 1000$ are mainly discussed in detail. And a schematic diagram for the distribution of the steady and unsteady solutions, obtained by time evolution calculations, is presented in the Dean number versus Grashof number plane (Dn–Gr) for $0 \leqslant Dn \leqslant 1000$ and $0 \leqslant Gr \leqslant 1000$.

4. Resistance coefficient and the Nusselt number

In the present study, the resistance coefficient λ is used as the representative quantity of the flow state. It is also called the *hydraulic resistance coefficient*, and is generally used in fluids engineering, defined as

$$\frac{P_1^* - P_2^*}{\Delta z^*} = \frac{\lambda}{d_h^*}\frac{1}{2}\rho\langle w^*\rangle^2 \tag{14}$$

where quantities with an asterisk denote dimensional ones, $\langle\ \rangle$ stands for the mean over the cross section of the rectangular duct, ρ the density, and $d_h^* = 4(2d \times 2dl)/(4d + 4dl)$ is the hydraulic diameter. The mean axial velocity $\langle w^*\rangle$ is calculated by

$$\langle w^*\rangle = \frac{\nu}{4\sqrt{2\delta}d}\int_{-1}^{1} \mathrm{d}x \int_{-1}^{1} w(x, y, t)\,\mathrm{d}y \tag{15}$$

Since $(P_1^* - P_2^*)/\Delta z^* = G$, λ is related to the mean nondimensional axial velocity $\langle w\rangle$ as

$$\lambda = \frac{8l\sqrt{2\delta}Dn}{(1+l)\langle w\rangle^2} \tag{16}$$

where $\langle w\rangle = \sqrt{2\delta}d\langle w^*\rangle/\nu$. In this paper, λ is used to discriminate the steady solution branches and to pursue the time evolution of the unsteady solutions. It should be remarked that $\lambda \propto Dn^{-1}$ in the limit of $Dn \to 0$ with δ keeping constant, since $\langle w\rangle \propto Dn$ in this limit.

The Nusselt number, Nu, which is used as an index of the heat transfer from the walls to the fluid, is defined as

$$Nu_c = \frac{1}{2}\int_{-1}^{1}\left[\frac{\partial T}{\partial x}\right]_{x=-1}\mathrm{d}y$$
$$Nu_h = \frac{1}{2}\int_{-1}^{1}\left[\frac{\partial T}{\partial x}\right]_{x=1}\mathrm{d}y \tag{17}$$

for steady solutions. For unsteady solutions, on the other hand, it is defined as

$$Nu_{\tau_c} = \frac{1}{2}\int_{-1}^{1}\left\langle\!\!\left\langle \left.\frac{\partial T}{\partial x}\right|_{x=-1}\right\rangle\!\!\right\rangle\mathrm{d}y$$
$$Nu_{\tau_h} = \frac{1}{2}\int_{-1}^{1}\left\langle\!\!\left\langle \left.\frac{\partial T}{\partial x}\right|_{x=1}\right\rangle\!\!\right\rangle\mathrm{d}y \tag{18}$$

where $\langle\!\langle\ \rangle\!\rangle$ denotes an average over a time interval τ. When the field is periodic, τ is taken as one period, and if it is chaotic τ is chosen as an appropriate time interval.

5. Results and discussion

5.1. Case I: $Gr = 500$

5.1.1. Steady solutions and their linear stability analysis

With the present numerical calculations, five branches of steady solutions are found for the Grashof number $Gr = 500$ over the range of the Dean number $0 \leqslant Dn \leqslant 1000$. They are shown in Fig. 2(a) for $100 \leqslant Dn \leqslant 1000$ using λ, the representative quantity for the bifurcation analysis of the solutions. The steady solution branches are named as the *first steady solution branch* (first branch, thick solid line), the *second steady solution branch* (second branch, thin solid line), the *third steady solution branch* (third branch, dash dotdot line), the *fourth steady solution branch* (fourth branch, dashed line) and the *fifth steady solution branch* (fifth branch, dash dotted line) respectively. In order to see the intricate branch structures as well as to distinguish the steady solution branches from each other, an enlargement of Fig. 2(a) is shown in Fig. 2(b) at larger Dean numbers, where it is observed that the steady solution branches are independent and there exists no bifurcating relation among the solution branches in the parameter range investigated in this paper. It should be noted that the lower portion of the third steady solution branch overlaps the first steady solution branch, as seen in Fig. 2(b). The steady solution branches are obtained using path continuation technique with various initial guess (for details, see Yanase et al. [19]), and the solution branches are distinguished by the nature and number of secondary flow vortices appearing in the cross section of the duct. It is found that the first branch is composed of one- and two-vortex solutions. The second branch consists of two- and four-vortex solutions. The third branch is characterized by two- and four-vortex solutions, but different from the second branch in the form of vortices near the outer wall. The fourth branch contains two-, four- and six-vortex solutions and the fifth branch two-, four-, six- and eight-vortex solutions.

Now, the accuracy of the numerical calculations is investigated for the truncation numbers M and N used in this paper. For good accuracy of the solutions, N is chosen equal to lM, where l is the aspect ratio of the duct cross section. The values of λ and $w(0,0)$, obtained at $Gr = 500$ and $Dn = 100$ for $l = 2$, are shown in Table 1 for various values of M and $N(= 2M)$, where $w(0,0)$ is the axial velocity at $(x, y) = (0,0)$. It is found that λ changes 0.00175% from $M = 14$ to $M = 16$, 0.00085% from $M = 16$ to $M = 18$, 0.00008% from $M = 18$ to $M = 20$ and 0.00001% from $M = 20$ to $M = 22$. $w(0,0)$ changes 0.055% from $M = 14$ to $M = 16$, 0.039% from $M = 16$ to $M = 18$, 0.029% from $M = 18$ to $M = 20$ and 0.013% from $M = 20$ to $M = 22$. Therefore, it is concluded that the values $M = 20$ and $N = 40$ give sufficient accuracy for the present numerical calculations.

The first steady solution branch is solely depicted in Fig. 3(a) for $10 \leqslant Dn \leqslant 1000$. This is the only branch which exists throughout the whole range of the Dean number of the present study. To observe the change of the flow patterns and temperature distributions, contours of typical secondary flow and temperature profile at several Dean numbers are shown in Fig. 3(b), where the contours of ψ and T are drawn with the increments $\Delta\psi = 0.6$ and $\Delta T = 0.2$ respectively. The same increments of ψ and T are used for all the figures in this paper, if not specified. Right-hand side of each box is

Table 1
The values of λ and $w(0,0)$ for various M and $N(= 2M)$ for $Gr = 500$ at $Dn = 100$

M	N	λ	$w(0,0)$
14	28	0.5637263	67.977
16	32	0.5637362	68.015
18	36	0.5637410	68.042
20	40	0.5637415	68.062
22	44	0.5637414	68.071

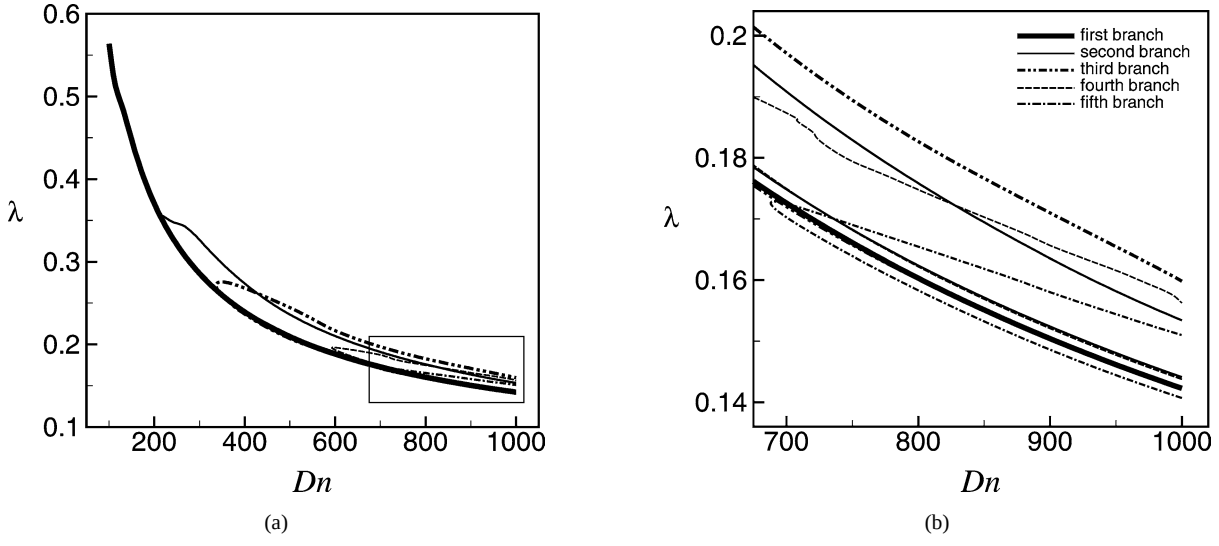

Fig. 2. (a) Steady solution branches for $Gr = 500$ and $100 \leqslant Dn \leqslant 1000$. (b) Enlargement of (a) at larger Dean numbers ($675 \leqslant Dn \leqslant 1000$).

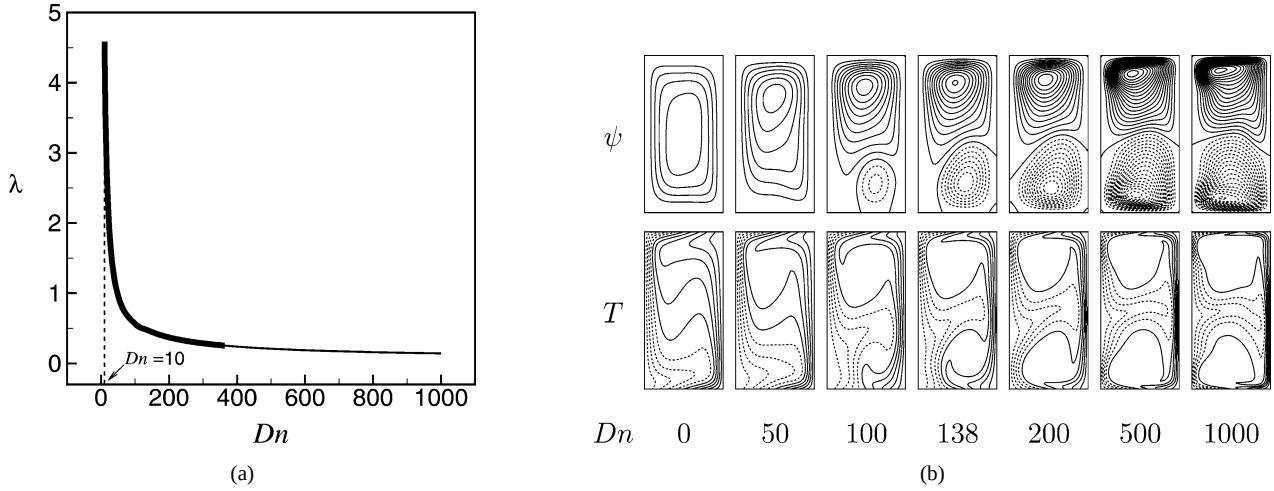

(a) (b)

Fig. 3. (a) First steady solution branch with the region of linear stability (bold line), (b) contours of secondary flow (top) and temperature profile (bottom) for the first steady solution branch for $Gr = 500$ and $0 \leqslant Dn \leqslant 1000$ ($\Delta\psi = 0.6$, $\Delta T = 0.2$).

in the outside direction of the duct curvature. In the figures of the secondary flow, solid lines (positive ψ) show that the secondary flow is in the counter clockwise direction while the dotted lines (negative ψ) in the clockwise direction. In the figures of the temperature field, solid lines are those for $T \geqslant 0$ and dotted ones for $T < 0$. As seen in Fig. 3(b), the first steady solution branch consists of one- and two-vortex solutions which are asymmetric with respect to the horizontal centre plane $y = 0$. Heating the outer wall causes deformation of the secondary flow and yields asymmetry of the flow. With the heating and cooling the sidewalls, changes of fluid density induce thermal convection in the fluid. The resulting flow behaviour in the cross section is, therefore, determined by the combined action of the radial flow caused by the centrifugal body force and the convection by the temperature difference. At smaller Dean numbers, the centrifugal body force is weaker and the thermal convection dominates the flow; the resulting flow consists of a single vortex which occupies the entire cross section. At larger Dean numbers, on the other hand, the centrifugal body force becomes stronger and the secondary flow is gradually re-built.

Linear stability of the steady solutions is then studied. It is found that among five branches of steady solutions, only a portion of the first steady solution branch is linearly stable, while all the others are linearly unstable. Table 2 shows the eigenvalues of the first steady solution branch, where the eigenvalues with the maximum real part of σ are presented. Those for the linearly stable solutions are printed in bold letters. As seen in Table 2, the stability region exists for the region $0 \leqslant Dn \leqslant 364.47$ and the perturbation grows oscillating ($\sigma_i \neq 0$) for $Dn \geqslant 364.48$. Linearly stable steady solution region is shown with a thick solid line in Fig. 3(a). It is found that the Hopf bifurcation takes place at $Dn \approx 364.47$.

5.1.2. Time evolution for Gr = 500

Time evolution calculations are performed for the Grashof number $Gr = 500$ at the Dean numbers $Dn = 100$, 400, 500 and 1000. It is found that the flow approaches a steady state monotonically for $Dn = 100$, where the initial condition is used from the first steady solution branch with a small perturbation. A single contour of the secondary flow and temperature profile for $Dn = 100$ at time $t = 8$ is shown in Fig. 4. It is found that the flow is a two-vortex solution which closely agrees with the steady solution on the first steady solution branch which is linearly stable. Time evolution of λ for $Dn = 400$ is shown in Fig. 5(a), using the initial condition from the second steady solution branch. This figure clearly shows that the flow is periodic for $Dn = 400$. In the same figure, to explore the relationship between the periodic solution and the steady states, steady values of λ on the steady

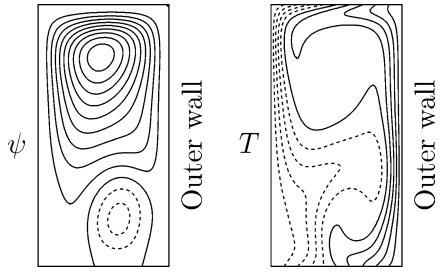

Fig. 4. Contour of secondary flow (left) and temperature profile (right) for $Gr = 500$ and $Dn = 100$ at $t = 8$ ($\Delta\psi = 0.6$, $\Delta T = 0.2$).

Table 2
Linear stability of the first steady solution branch for $Gr = 500$

Dn	λ	σ_r	σ_i
0	**0.000000**	$\mathbf{-7.392 \times 10^{-1}}$	**0**
50	**0.963474**	$\mathbf{-7.356 \times 10^{-1}}$	**0**
150	**0.447578**	$\mathbf{-3.434 \times 10^{-1}}$	**0**
300	**0.285783**	$\mathbf{-6.198 \times 10^{-1}}$	**0**
364.47	**0.253199**	$\mathbf{-2.550 \times 10^{-4}}$	$\mathbf{\pm 2.816 \times 10}$
364.48	0.253195	4.986×10^{-4}	$\pm 2.816 \times 10$
365	0.252973	3.971×10^{-2}	$\pm 2.818 \times 10$
500	0.209231	1.129×10	$\pm 3.196 \times 10$
1000	0.142268	4.936×10	$\pm 5.296 \times 10$

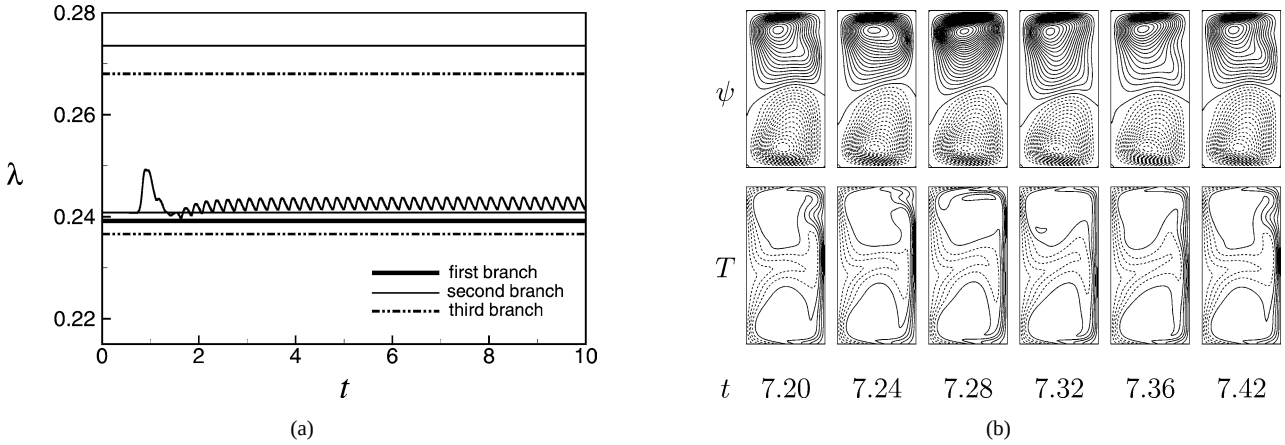

Fig. 5. The results for $Gr = 500$ and $Dn = 400$. (a) Time evolution of λ and the values of λ for the steady solutions at $0 \leqslant t \leqslant 10$, (b) contours of secondary flow (top) and temperature profile (bottom) for one period of oscillation at $7.20 \leqslant t \leqslant 7.42$ ($\Delta\psi = 0.6$, $\Delta T = 0.2$). Time is non-dimensionalized, as is in all the figures appearing henceforth.

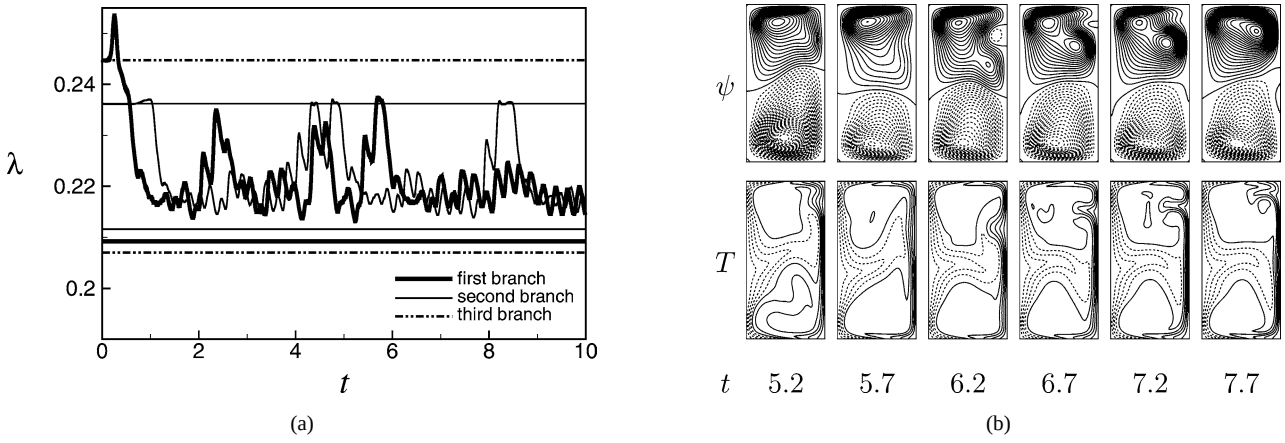

Fig. 6. The results for $Gr = 500$ and $Dn = 500$. (a) Time evolution of λ and the values of λ for the steady solutions at $0 \leqslant t \leqslant 10$, (b) contours of secondary flow (top) and temperature profile (bottom) for $5.2 \leqslant t \leqslant 7.7$ ($\Delta\psi = 0.6$, $\Delta T = 0.2$).

solution branches at $Dn = 400$ are also shown which are indicated by straight lines using the same kind of lines as were used in the bifurcation diagram in Fig. 2. As seen in Fig. 5(a), the periodic solution oscillates around $\lambda = 0.2427$ in the region between the second and third steady solution branch and the second steady solution branch ($\lambda = 0.2408$) is seen to be a lower bound of this oscillation. To observe the change of the flow characteristics, as time proceeds, contours of secondary flow and temperature profile for $Dn = 400$ are shown in Fig. 5(b), for one period of oscillation, at $7.20 \leqslant t \leqslant 7.42$. Fig. 5(b) shows that the periodic oscillation at $Dn = 400$ is a two-vortex solution.

Next, time evolution of λ together with the values of λ for the steady solution branches, indicated by straight lines, are shown for $Dn = 500$ and 1000 in Figs. 6(a) and 7(a), respectively. Figs. 6(a) and 7(a) show that the flow oscillates irregularly which suggests that the flow is chaotic for both of the cases. It is noted that the chaotic solution at $Dn = 500$ drifts around $\lambda = 0.22$ between the upper and lower parts of the second steady solution branch. Initial condition independence for the chaotic solution at $Dn = 500$ has also been examined, and it is found that the chaotic solution moves around the same place ($\lambda \approx 0.22$) though two different initial conditions were used from two steady solutions. On the other hand, the chaotic solution at $Dn = 1000$, where the initial condition is used from the third steady solution branch, moves around $\lambda = 0.1655$ above all the steady solution branches and the steady solution branch having the maximum λ ($\lambda = 0.1603$, upper part of the third steady solution branch) looks like an envelope of this chaotic solution. Thus it is suggested that occurrence of the chaotic state is related with destabilization of the steady solutions, which reminds us the case of Lorenz chaos [20]. To observe the change of the flow pattern, contours of typical secondary flow and temperature profile are shown for $Dn = 500$ at $6.1 \leqslant t \leqslant 7.6$ and for $Dn = 1000$ at $4.0 \leqslant t \leqslant 6.0$ in Figs. 6(b) and 7(b) respectively, where the increments $\Delta\psi = 1.2$ and $\Delta T = 0.4$ are used for $Dn = 1000$. As seen in the secondary flow patterns, multi-vortex solution is observed for the chaotic solutions ($Dn = 500$ and 1000) though a two-vortex solution is found for the steady-state ($Dn = 100$) and periodic solutions ($Dn = 400$).

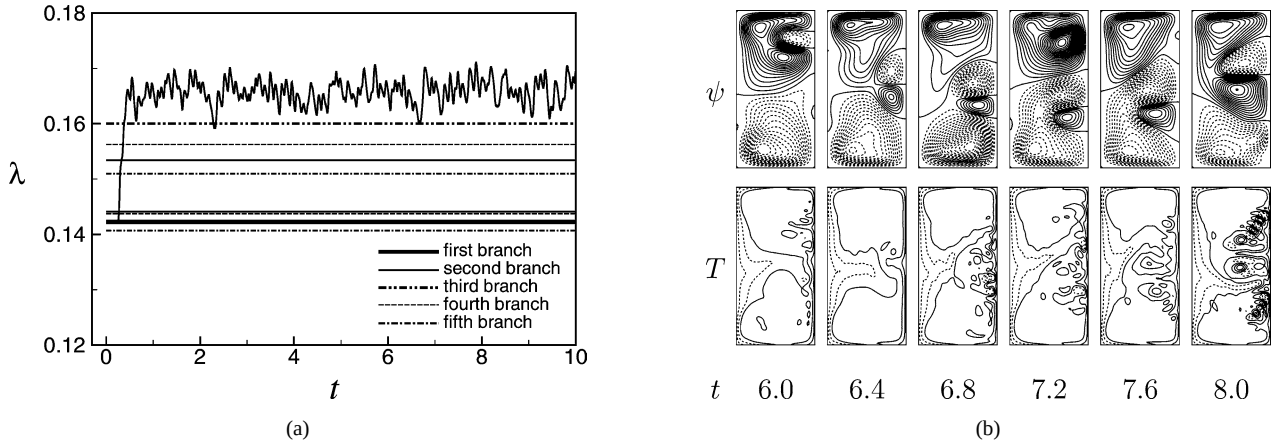

Fig. 7. The results for $Gr = 500$ and $Dn = 1000$. (a) Time evolution of λ and the values of λ for the steady solutions at $0 \leqslant t \leqslant 10$, (b) contours of secondary flow (top) and temperature profile (bottom) for $6.0 \leqslant t \leqslant 8.0$ ($\Delta\psi = 1.2$, $\Delta T = 0.4$).

5.1.3. Nusselt number

The Nusselt number, *Nu*, defined in Eq. (17), can be used as an index of the convective heat transfer from the walls to the flow. If the flow field is not steady, time-average of the Nusselt number, Nu_τ, is used which is defined in Eq. (18). To study the convective heat transfer for differentially heated vertical sidewalls, variation of the Nusselt number with the Dean number is shown in Fig. 8 for the first steady solution branch, where a thick solid line denotes Nu_c on the inner sidewall and a thin solid line Nu_h on the outer sidewall. Since among the steady solution branches obtained only the first steady solution branch is linearly stable, calculation of the steady values of the Nusselt number is meaningful only for this branch. The time-average of *Nu*, calculated by the time evolution computations on the inner and outer sidewalls at several values of the Dean number, is also shown in the same figure. In order to study the details of the heat transfer from the walls to the fluid, temperature gradients on the inner and outer sidewalls are calculated which are shown in Fig. 9(a) and (b), respectively.

The behavior of the Nusselt number, as the Dean number increases from zero, is now discussed by examination of Figs. 8 and 9. As seen in Fig. 8, the values of the Nusselt number are different on both the sidewalls for $Dn = 0$. On the inner sidewall the Nusselt number is larger than that on the outer sidewall. This is due to the bend of the duct. The relative magnitude of the Nusselt number, however, reverses as the Dean number increases as seen in Fig. 8. This behavior can be understood if the profiles of the temperature gradient $\frac{\partial T}{\partial x}$ on both sidewalls are studied. In Fig. 9(a), it is shown that $\frac{\partial T}{\partial x}$ on the inner (cooled) sidewall decreases in the central region around $y = 0$ as the Dean number increases. It is easily found from Fig. 3(b) that this is caused by the advection of the secondary flow in the outward direction around $y = 0$ due to the centrifugal force. It is also shown in the same figure that $\frac{\partial T}{\partial x}$ tends to increase in the regions other than the central region when the Dean number becomes greater than 100. This is caused by the advection of the secondary flow in the inward direction there, which is a

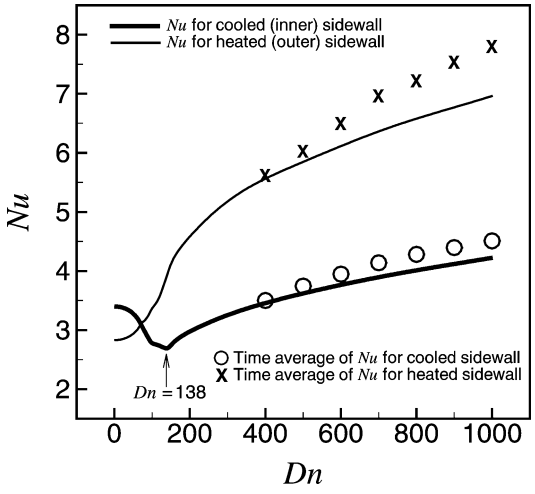

Fig. 8. Variation of the Nusselt number with the Dean number for the first steady solution branch for $Gr = 500$.

reverse flow of the outward secondary flow in the central region. Since the decrease of the Nusselt number in the central region is stronger than the increase of the Nusselt number in the other regions for small Dean numbers, the Nusselt number on the inner sidewall decreases as the Dean number goes up from zero. However, as the Dean number exceeds a critical value $Dn_c \approx 138$, the increase of $\frac{\partial T}{\partial x}$ in the upper and lower regions overwhelms the decrease of $\frac{\partial T}{\partial x}$ in the central region, so *Nu* begins to increase on the inner sidewall. As seen in Fig. 9(b), which shows the temperature gradient on the outer (heated) sidewall, $\frac{\partial T}{\partial x}$ increases, as the Dean number goes up, over the whole region except for small Dean numbers. This is because the secondary flow enhances $\frac{\partial T}{\partial x}$ not only in the central region but in other regions as well if the Dean number is greater than 100. Even for small Dean numbers $\frac{\partial T}{\partial x}$ increases remarkably in the upper and lower regions, and then *Nu* monotonically increases as the Dean number goes up from zero.

Time-average of the Nusselt number, obtained by the time evolution computation of the Nusselt number for the inner

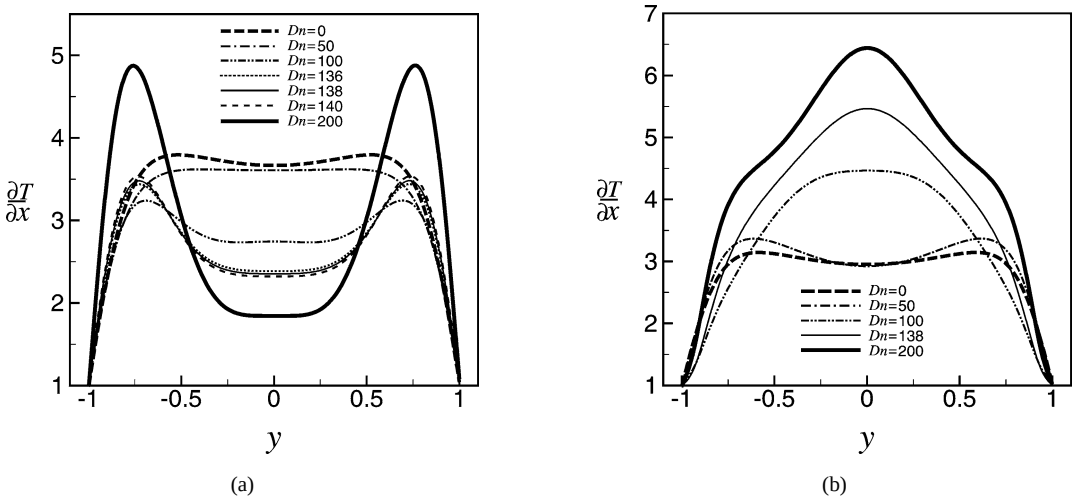

Fig. 9. Temperature gradient for $Gr = 500$. (a) At the cooled sidewall, (b) at the heated sidewall.

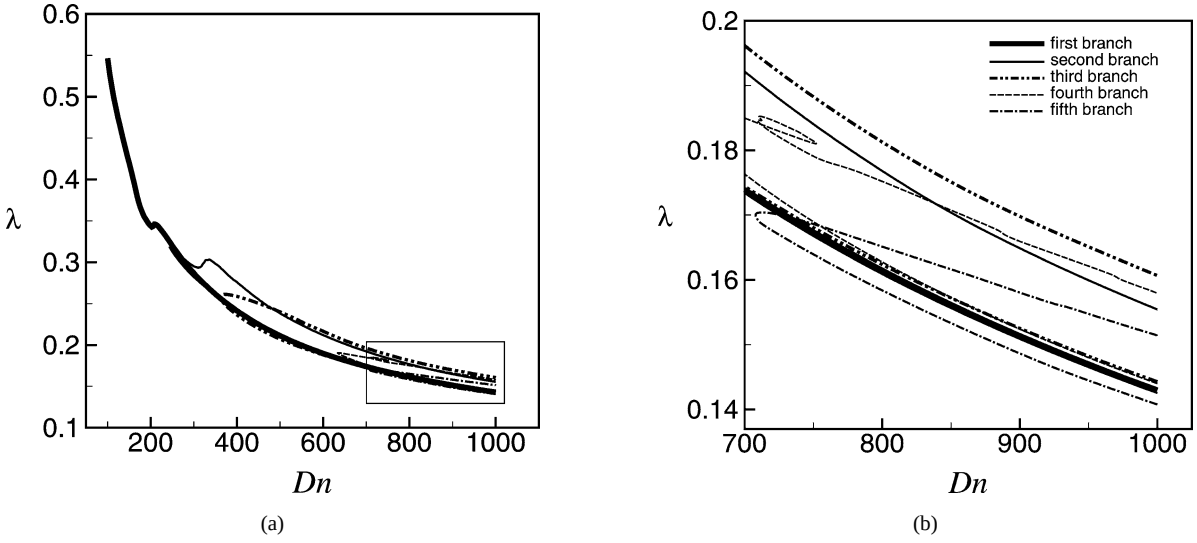

Fig. 10. (a) Steady solution branches for $Gr = 1000$ and $100 \leqslant Dn \leqslant 1000$. (b) Enlargement of (a) at larger Dean numbers ($700 \leqslant Dn \leqslant 1000$).

and outer sidewalls, is calculated at several values of the Dean number for both the periodic and chaotic solutions and plotted with the steady values of the Nusselt number in Fig. 8. As seen in Fig. 8, time-averaged values of the Nusselt number are larger than the steady values of the Nusselt number on the first steady solution branch for both the inner and outer sidewalls, which suggests that occurrence of periodic or chaotic flow enhances heat transfer in the flow. It should be remarked that the tendency of increasing the Nusselt number is larger on the outer sidewall than that on the inner sidewall for larger Dean numbers, which can be explained by the fact that many subsidiary secondary vortices are generated near the outer sidewall [18].

5.2. *Case II:* $Gr = 1000$

5.2.1. *Steady solutions and their linear stability analysis*

After a comprehensive survey over the range of the parameters, five branches of steady solutions are found for the Grashof number $Gr = 1000$ over the Dean number $0 \leqslant Dn \leqslant 1000$. They are shown in Fig. 10(a) for $100 \leqslant Dn \leqslant 1000$. The steady solution branches are named, as they were called for $Gr = 500$, the *first steady solution branch* (first branch, thick solid line), the *second steady solution branch* (second branch, thin solid line), the *third steady solution branch* (third branch, dash dotdot line), the *fourth steady solution branch* (fourth branch, dashed line) and the *fifth steady solution branch* (fifth branch, dash dotted line) respectively. To individualize the steady solution branches, an enlargement of Fig. 10(a) is shown in Fig. 10(b) for larger Dean numbers ($700 \leqslant Dn \leqslant 1000$) where it is observed that there exists no bifurcating relation among the steady solution branches in the parameter range investigated in this paper. However, it is noticed that the lower part of the second steady solution branch overlaps the first steady solution branch, and the lower part of the third steady solution branch is very close to that of the fourth steady solution branch at larger Dean numbers. The steady solution branches are

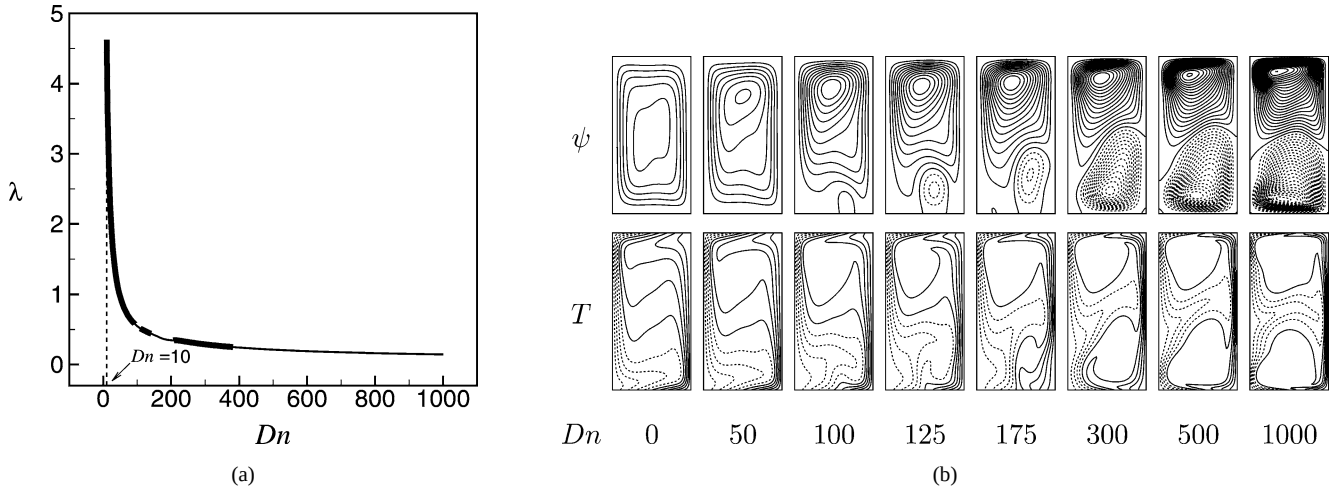

Fig. 11. (a) First steady solution branch with the regions of linear stability (bold line), (b) contours of secondary flow (top) and temperature profile (bottom) for the first steady solution branch for $Gr = 1000$ and $0 \leqslant Dn \leqslant 1000$ ($\Delta\psi = 0.6$, $\Delta T = 0.2$).

differentiated by the nature and number of secondary flow vortices appearing in the cross section of the duct, and it is found that the secondary flow patterns on the steady solution branches for $Gr = 1000$ are qualitatively similar to those for $Gr = 500$.

The first steady solution branch is exclusively depicted in Fig. 11(a) for $10 \leqslant Dn \leqslant 1000$, and the contours of typical secondary flow and temperature profile at several values of the Dean number in Fig. 11(b). In Fig. 11(b), to plot the contours of ψ and T, the increments $\Delta\psi$ and ΔT are taken the same as were considered for the case of $Gr = 500$. As seen in Fig. 11(b), the secondary flow is in the form of one-vortex and asymmetric two-vortex solutions. Similar forms of vortices were also found for the respective branch for $Gr = 500$. Then linear stability of the steady solutions is investigated. It is found that among five branches of steady solutions only the first steady solution branch is linearly stable in three different intervals of the Dean number, while all the other steady solution branches are linearly unstable. Eigenvalues with the maximum real part of σ of the first steady solution branch are shown in Table 3. In Table 3, the eigenvalues for the linearly stable solutions are printed in bold letters. As seen in Table 3, stability regions exist for $0 \leqslant Dn \leqslant 93.276$, $108.173 \leqslant Dn \leqslant 141.24$ and $206 \leqslant Dn \leqslant 382.874$, and the perturbation grows oscillating ($\sigma_i \neq 0$) for $93.277 \leqslant Dn \leqslant 108.172$, $141.25 \leqslant Dn \leqslant 205.998$ and $Dn \geqslant 382.875$. Linearly stable steady solution regions are shown with thick solid lines in Fig. 11(a). It is found that the Hopf bifurcation takes place at $Dn \approx 93.276$, $Dn \approx 108.173$ and $Dn \approx 382.874$.

Table 3
Linear stability of the first steady solution branch for $Gr = 1000$

Dn	λ	σ_r	σ_i
0	**0.000000**	$\mathbf{-8.456 \times 10^{-1}}$	**0**
50	**0.961952**	$\mathbf{-8.642 \times 10^{-1}}$	**0**
93.276	**0.574974**	$\mathbf{-3.830 \times 10^{-5}}$	$\mathbf{\pm 5.484}$
93.277	0.574969	2.204×10^{-5}	± 5.484
100	0.546435	8.069×10^{-1}	± 5.845
108.172	0.516880	1.553×10^{-5}	± 7.312
108.173	**0.516876**	$\mathbf{-1.188 \times 10^{-5}}$	$\mathbf{\pm 7.313}$
125	**0.473229**	$\mathbf{-9.514 \times 10^{-1}}$	**0**
141.24	**0.437981**	$\mathbf{-8.572 \times 10^{-4}}$	$\mathbf{\pm 1.095 \times 10}$
141.25	0.437960	4.451×10^{-5}	$\pm 1.095 \times 10$
200	0.343613	4.583	± 3.091
205.998	0.342926	6.092×10^{-4}	± 1.438
206	**0.342929**	$\mathbf{-7.104 \times 10^{-4}}$	$\mathbf{\pm 1.436}$
250	**0.320104**	$\mathbf{-4.959 \times 10^{-1}}$	**0**
300	**0.286776**	$\mathbf{-4.866 \times 10^{-1}}$	**0**
382.874	**0.247772**	$\mathbf{-1.326 \times 10^{-5}}$	$\mathbf{\pm 3.513 \times 10}$
382.875	0.247771	7.976×10^{-6}	$\pm 3.513 \times 10$
500	0.211197	6.401	$\pm 3.895 \times 10$
1000	0.142989	4.685×10	$\pm 5.818 \times 10$

5.2.2. Time evolution for $Gr = 1000$

In order to study the nonlinear behavior of the unsteady solutions, time evolution calculations of the velocity and temperature fields are performed for the Grashof number $Gr = 1000$ at the Dean numbers Dn =50, 100, 125, 175, 300, 500 and 1000. It is found that the solution approaches a single vortex steady-state solution monotonically for $Dn =$ 50, whatever the initial condition is. Time evolutions of λ for $Dn = 100$ and 175, using the initial conditions on the first steady solution branch, are then studied as shown in Figs. 12(a) and 13(a), respectively, where it is seen that the flow is periodic for both $Dn = 100$ and 175 but different in nature. It is noted that time evolution of λ for $Dn = 125$ shows that the flow is steady. To explore the relationship between the periodic solution and the steady state, the values of λ on the first steady solution branch at $Dn = 100$ and 175 are also shown with straight lines in the respective figures. It is observed that the periodic solution at $Dn = 100$ oscillates along the first steady solution branch ($\lambda \approx 0.5464$), whereas the periodic solution at $Dn = 175$ oscillates multiperiodically above the first steady solution branch, and the branch seems to be an envelope of this periodic solu-

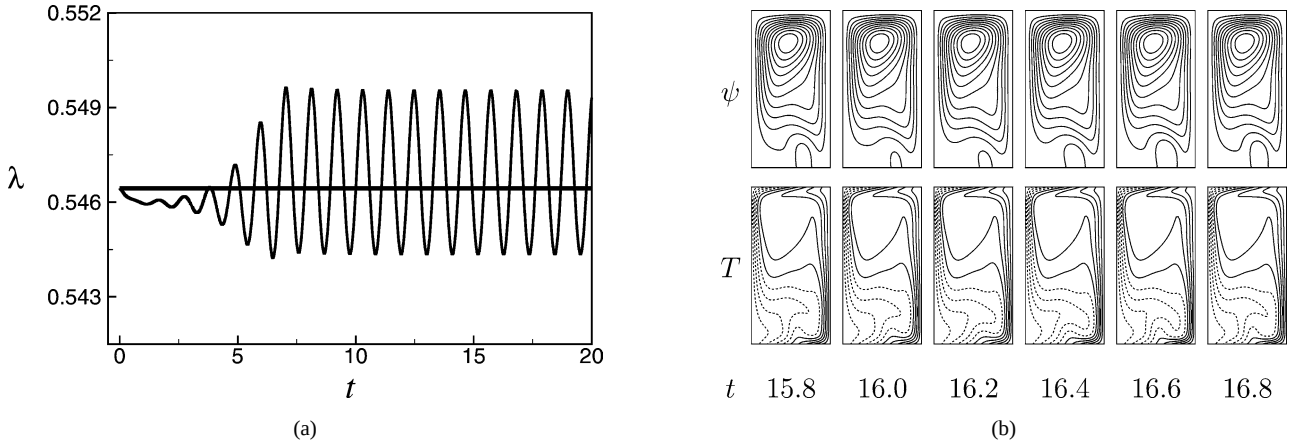

(a) (b)

Fig. 12. The results for $Gr = 1000$ and $Dn = 100$. (a) Time evolution of λ and the value of λ for the steady solution at $0 \leqslant t \leqslant 20$, (b) contours of secondary flow (top) and temperature profile (bottom) for one period of oscillation at $15.8 \leqslant t \leqslant 16.8$ ($\Delta\psi = 0.6$, $\Delta T = 0.2$).

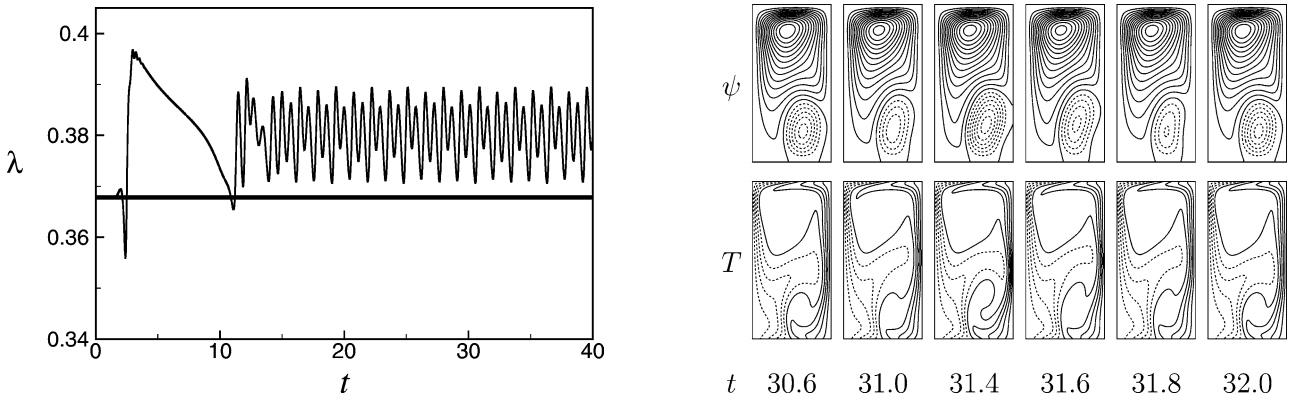

(a) (b)

Fig. 13. The results for $Gr = 1000$ and $Dn = 175$. (a) Time evolution of λ and the value of λ for the steady solution at $0 \leqslant t \leqslant 40$, (b) contours of secondary flow (top) and temperature profile (bottom) for one period of oscillation at $30.6 \leqslant t \leqslant 32.0$ ($\Delta\psi = 0.6$, $\Delta T = 0.2$).

tion. To observe the periodic change of the flow pattern, contours of typical secondary flow and temperature profile for one period of oscillation are drawn for $Dn = 100$ at $15.8 \leqslant t \leqslant 16.8$ and for $Dn = 175$ at $30.6 \leqslant t \leqslant 32.0$ in Figs. 12(b) and 13(b) respectively, where it is found that the periodic oscillations are of two-vortex solution with one large vortex dominating the other one, and as the Dean number becomes large the smaller vortex expands gently, which resembles the change of the flow pattern on the first steady solution branch shown in Fig. 11(b). Time evolutions of λ for $Dn = 300$ show that the flow is steady like the case of $Dn = 50$ and 125. Linear stability analysis also reveals that the steady solution is linearly stable at Dn =50, 125 and 300, and that the periodic solutions in the unstable regions result from the Hopf bifurcation on the first steady solution branch.

Next, time evolution of λ is performed for $Dn = 500$, using the initial condition on the second steady solution branch, as shown in Fig. 14(a), where it is found that the flow again turns into time periodic. In Fig. 14(a), the values of λ for all the steady solution branches at $Dn = 500$ are also shown, which are indicated by straight lines using the same kind of lines as were used in the bifurcation diagram in Fig. 10. As seen in Fig. 14(a), the periodic solution at $Dn = 500$ drifts around $\lambda = 0.2182$ in the region between the upper and lower parts of the second steady solution branch. In this regard it should be noted that though a chaotic solution was found for a moderate Grashof number ($Gr = 500$) at $Dn = 500$, for a larger Grashof number ($Gr = 1000$), on the other hand, the periodic solution is observed at the same Dean number ($Dn = 500$). Contours of typical secondary flow and temperature profile are shown for $Dn = 500$, for one period of oscillation, at $6.97 \leqslant t \leqslant 7.17$ in Fig. 14(b). As seen in Fig. 14(b), the periodic solution at $Dn = 500$ is a two-vortex solution. Time evolution of λ is then performed for $Dn = 1000$ using the initial condition from the third steady solution branch, as shown in Fig. 15(a). In this figure, the time evolution computation together with the values of λ for all the steady solution branches at $Dn = 1000$, indicated by straight lines, are plotted. It is seen that the flow oscillates irregularly around $\lambda = 0.165$, which suggests that the flow is chaotic. Initial condition independence has also been examined using the initial condition from the second steady solution branch, and it is observed that the

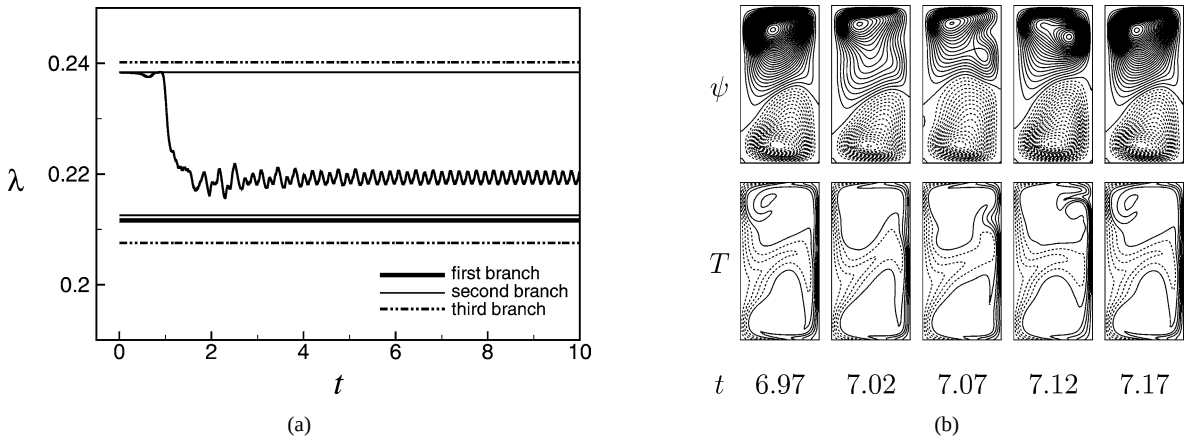

(a) (b)

Fig. 14. The results for $Gr = 1000$ and $Dn = 500$. (a) Time evolution of λ and the values of λ for the steady solutions at $0 \leqslant t \leqslant 10$, (b) contours of secondary flow (top) and temperature profile (bottom) for one period of oscillation at $6.97 \leqslant t \leqslant 7.17$ ($\Delta\psi = 0.6$, $\Delta T = 0.2$).

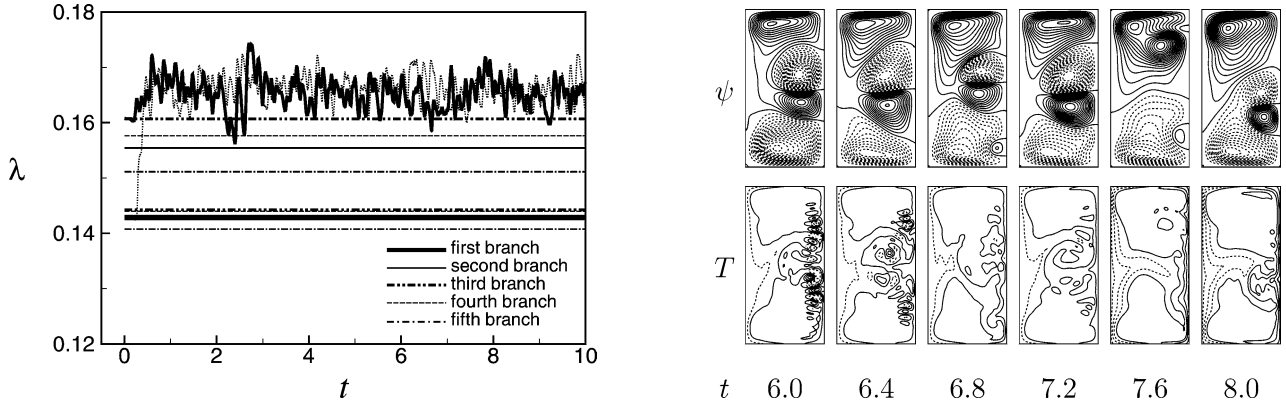

(a) (b)

Fig. 15. The results for $Gr = 1000$ and $Dn = 1000$. (a) Time evolution of λ and the values of λ for the steady solutions at $0 \leqslant t \leqslant 10$, (b) contours of secondary flow (top) and temperature profile (bottom) for $6.0 \leqslant t \leqslant 8.0$ ($\Delta\psi = 1.2$, $\Delta T = 0.4$).

chaotic solution moves around the same place ($\lambda \approx 0.165$) above all the steady solution branches, like the case for $Gr = 500$ at $Dn = 1000$. To observe the irregular change of the chaotic flow behavior, as time proceeds, contours of secondary flow and temperature profile for $Dn = 1000$ are shown in Fig. 15(b) for $6.0 \leqslant t \leqslant 8.0$, where the increments $\Delta\psi = 1.2$ and $\Delta T = 0.4$ are used. As seen in the secondary flow patterns, a four-vortex solution is found for the chaotic solution at $Dn = 1000$ as also found for $Gr = 500$ at $Dn = 1000$.

It is interesting to note that in the linearly unstable regions, periodic solutions develop in three different intervals of the Dean number, $93.28 \leqslant Dn \leqslant 108.17$, $141.25 \leqslant Dn \leqslant 205.99$ and $382.87 \leqslant Dn \leqslant 565$, and the flow undergoes the scenario *steady–periodic–steady–periodic–steady–periodic–chaotic*, when the Dean number is increased. It is found that the three periodic solutions are quite different in the form of secondary flow patterns as seen in Figs. 12–14. These periodic solutions are thought to be related to the branches of the periodic solutions bifurcating from the Hopf bifurcation point.

5.2.3. Nusselt number

Since among the steady solution branches obtained, only the first branch is linearly stable, steady values of the Nusselt number for $Gr = 1000$ are calculated only for this branch. Variation of the Nusselt number with the Dean number is shown in Fig. 16, where a thick solid line denotes Nu_c on the inner sidewall and a thin solid line Nu_h on the outer sidewall. In order to study the phenomena for the convective heat transfer from the walls to the fluid, temperature gradients on the outer and inner sidewalls are also calculated though they are not shown here. It is found that the behavior of the steady values of the Nusselt number and that of the temperature gradients $\frac{\partial T}{\partial x}$ on both the inner and outer sidewalls for $Gr = 1000$ are nearly the same as that of the case for $Gr = 500$.

Time-average of the Nusselt number on the inner and outer sidewalls at several values of the Dean number are calculated for both the periodic and chaotic solutions, and plotted with the steady values of the Nusselt number in Fig. 16. Though the results are nearly similar to those of the case for $Gr = 500$, it must be noticed that the increase of the Nus-

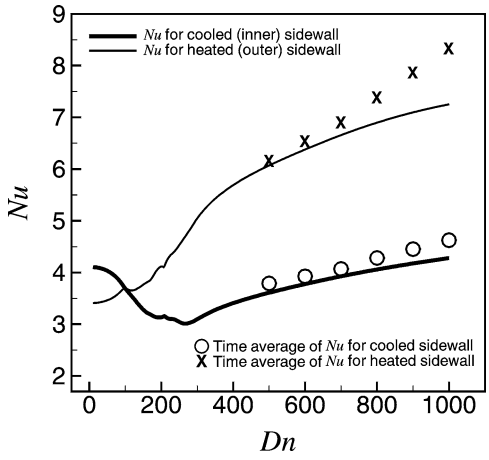

Fig. 16. Variation of the Nusselt number with the Dean number for the first steady solution branch for $Gr = 1000$.

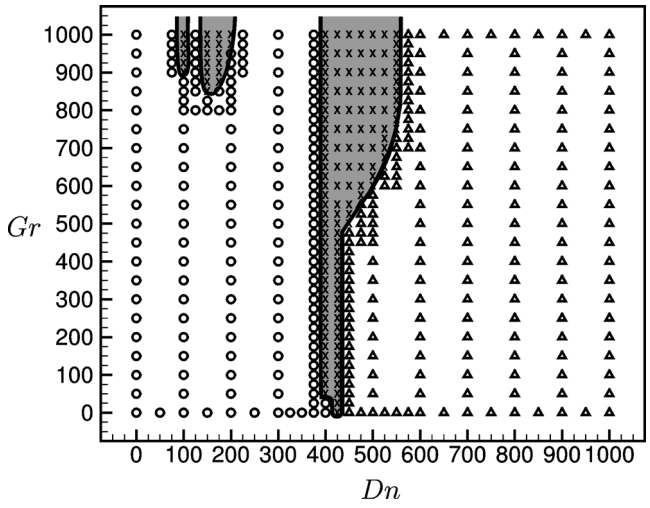

Fig. 17. Distribution of the time-dependent solutions in the Dean number versus Grashof number ($Dn - Gr$) plane for $0 \leqslant Dn \leqslant 1000$ and $0 \leqslant Gr \leqslant 1000$ (○: steady-state solution, ×: periodic solution (shaded regions), △: chaotic solution and solid lines are the rough boundaries of the periodic solutions).

selt number from the steady values takes place for larger Dean numbers compared with the case for $Gr = 500$. This is because the flow becomes chaotic for relatively small Dean numbers at lower Grashof numbers, whereas it remains periodic for higher Grashof numbers. Thus, it is concluded that chaotic states enhance heat transfer more effectively than periodic states. From Figs. 8 and 16, it is seen that the increase of the Dean number leads to gradual enhancement of the Nusselt number. To compare the convective heat transfer of a curved duct with that of a straight channel, an additional calculation of the Nusselt number for a straight channel is conducted. It is found that at the specific Dean number, $Dn = 600$, which is equivalent to the Reynolds number $Re = Dn/\sqrt{2\delta} = 1342$, the Nusselt number on the outher sidewall for the curved duct is approximately 100% larger than that of the corresponding straight channel.

5.2.4. Phase diagram in the Dn–Gr plane

Finally, the distribution of the time-dependent solutions, obtained by the time evolution calculations of the flow, is shown in Fig. 17 in the Dean number versus Grashof number (Dn–Gr) plane for $0 \leqslant Dn \leqslant 1000$ and $0 \leqslant Gr \leqslant 1000$, where the regions of periodic solutions are displayed with shading surrounded by solid boundaries. As seen in Fig. 17, the steady flow turns into chaos through periodic flows as the Dean number increases keeping the Grashof number fixed. However, for larger Grashof numbers ($Gr > 850$), it is observed that there exist three exclusive regions of the Dean number where the solution is time periodic. If the Dean number is increased further, the solution becomes chaotic no matter what the Grashof number is. It is interesting to note that for larger Grashof numbers, the regions of periodic solutions increase while the occurrence of chaotic states is slightly delayed as the Dean number increases. However, as the Grashof number increases further, the region of periodic solutions expands gradually and the three regions of periodic solutions merge into a single region of periodic solutions when $Gr > 2000$.

6. Conclusions

A detailed numerical study of the non-isothermal flows through a curved rectangular duct of aspect ratio 2 has been conducted with consideration of convective heat transfer by use of the spectral method. In the present study, a temperature difference is applied between the vertical outer and inner sidewalls, where the outer wall is heated and the inner one is cooled. In this paper, numerical computations of the flow characteristics are performed over a wide range of the Dean number $0 \leqslant Dn \leqslant 1000$ for the Grashof numbers $100 < Gr \leqslant 1000$, among which two cases of the Grashof numbers $Gr = 500$ and $Gr = 1000$ are studied in detail.

After a comprehensive survey over the range of the parameters, five branches of asymmetric steady solutions are found for both $Gr = 500$ and 1000. Linear stability with respect to two-dimensional perturbations reveals an important as well as unexpected results. It is found that among five branches of steady solutions only a limited portion of the first steady solution branch is linearly stable in a single interval of the Dean number for $Gr = 500$. The same branch is found to be linearly stable in three different intervals of the Dean number for $Gr = 1000$, and there exists no linearly stable region in any other steady solution branch. It is found that the Hopf bifurcation and inverse Hopf bifurcation occur at the Dean numbers of the boundaries between the stable and unstable regions. Time evolution calculations of the flow show that for $Gr = 500$, the laminar flow turns into chaos through time periodic states in a straightforward way "*steady–periodic–chaotic*", for $Gr = 1000$, on the other hand, the flow undergoes "*steady–periodic–steady–periodic–steady–periodic–chaotic*", as the Dean number is increased. It is worth mentioning that irregular oscillation of isothermal flows through a curved rectangular duct has

been observed experimentally by Ligrani and Niver [6] for the large aspect ratio.

Steady values of the Nusselt number, calculated for the first steady solution branch, show that the larger the Dean number is, the larger the Nusselt number on the outer sidewall becomes. An interesting finding noticed for $Gr = 1000$ is that, the increase of the Nusselt number from the steady values takes place for larger Dean numbers compared with the case for $Gr = 500$. This is due to the suppressing effect on the transition to chaos by the Grashof number, whereas the transition is induced by increasing the Dean number. Time-averaged values of the Nusselt number have also been calculated for cases when the field is periodic or chaotic, and consequently it is suggested that the periodic or chaotic flow enhances heat transfer more effectively. The rate of convective heat transfer at the outer sidewall is found to be much higher than that in a straight channel, and is seen to increase as secondary flow activities become stronger.

In the present study, only two-dimensional velocity and temperature field, uniform along the duct, is treated mainly for two reasons. Firstly, two-dimensional field is used as the basis for three-dimensional analysis, and secondly, various types of two-dimensional solutions give good sign of three-dimensional behavior of the field. Stable steady solutions may correspond to steady state realized in the downstream of the duct, periodic solutions to three-dimensional oscillating solutions, and chaotic solution indicates more intricate three-dimensional turbulence.

Acknowledgements

Rabindra Nath Mondal, one of the authors, would gratefully like to acknowledge the financial support from the Japanese Ministry of Education, Culture, Sports, Science and Technology (Monbukagakusho) for study in Japan.

References

[1] S.C.R. Dennis, M. Ng, Dual solutions for steady laminar flow through a curved tube, Quart. J. Mech. Appl. Math. 35 (1982) 305–324.
[2] Z. Yang, H.B. Keller, Multiple laminar flows through curved pipes, Appl. Numer. Math. 2 (1986) 257–271.
[3] S. Yanase, N. Goto, K. Yamamoto, Dual solutions of the flow through a curved tube, Fluid Dyn. Res. 14 (1989) 191–201.
[4] K. Nandakumar, J.H. Masliyah, Bifurcation in steady laminar flow through curved tubes, J. Fluid Mech. 119 (1982) 475–490.
[5] H.C. Kao, Some aspects of bifurcation structure of laminar flow in curved ducts, J. Fluid Mech. 243 (1992) 519–539.
[6] P.M. Ligrani, R.D. Niver, Flow visualization of Dean vortices in a curved channel with 40 to 1 aspect ratio, Phys. Fluids 31 (1988) 3605–3617.
[7] S. Yanase, K. Nishiyama, On the bifurcation of laminar flows through a curved rectangular tube, J. Phys. Soc. Japan 57 (1988) 3790–3795.
[8] S. Thangam, N. Hur, Laminar secondary flows in curved rectangular ducts, J. Fluid Mech. 217 (1990) 421–440.
[9] W.H. Finlay, K. Nandakumar, Onset of two-dimensional cellular flow in finite curved channels of large aspect ratio, Phys. Fluids A 2 (1990) 1163–1174.
[10] K.H. Winters, A bifurcation study of laminar flow in a curved tube of rectangular cross-section, J. Fluid Mech. 180 (1987) 343–369.
[11] S. Yanase, Y. Kaga, R. Daikai, Laminar flows through a curved rectangular duct over a wide range of the aspect ratio, Fluid Dyn. Res. 31 (2002) 151–183.
[12] K.C. Cheng, M. Akiyama, Laminar forced convection heat transfer in curved rectangular channels, Internat. J. Heat Mass Transfer 13 (1970) 471–490.
[13] Y. Mori, Y. Uchida, T. Ukon, Forced convective heat transfer in curved channel with a square cross section, Internat. J. Heat Mass Transfer 14 (1971) 1787–1805.
[14] G. Yee, R. Chilukuri, J.A.C. Humphrey, Developing flow and heat transfer in strongly curved ducts of rectangular cross section, ASME J. Heat Transfer 102 (1980) 285–291.
[15] Y. Komiyama, F. Mikami, K. Okui, Laminar forced convection heat transfer in curved channel of rectangular cross section, Trans. JSME Ser. B 50 (1984) 424–434.
[16] Y. Ru, S.F. Chang, Combined free and forced convection for developed flow in curved pipes with finite curvature ratio, Internat. J. Heat Fluid Flow 15 (6) (1994) 470–476.
[17] P.M. Ligrani, S. Choi, A.R. Scallert, P. Skogerboe, Effects of Dean vortex pairs on surface heat transfer in curved channel flow, Internat. J. Heat Mass Transfer 39 (1996) 27–37.
[18] T.T. Chandratilleke, Nursubyakto, Numerical prediction of secondary flow and convective heat transfer in externally heated curved rectangular ducts, Internat. J. Thermal Sci. 42 (2003) 187–198.
[19] S. Yanase, R.N. Mondal, Y. Kaga, K. Yamamoto, Transition from steady to chaotic states of isothermal and non-isothermal flows through a curved rectangular duct, J. Phys. Soc. Japan 74 (1) (2005) 345–358.
[20] E.N. Lorenz, Deterministic nonperiodic flow, J. Atmos. Sci. 20 (1963) 130–141.